Proceedings World Geothermal Congress 2015
Melbourne, Australia, 19-25 April 2015

An Innovative Reservoir Engineering Program for Assessing EGSs in Australian Conditions

Nima GHOLIZADEH DOONECHALY[a], Reda ABDEL AZIM[a], Sheik S. RAHMAN[a], Stephen TYSON[b] and Klaus REGENAUER-LIEB[a]

a-University of New south Wales, Sydney

b-University of Queensland, Brisbane

sheik.rahman@unsw.edu.au

Keywords: crystalline basement, enhanced geothermal system, creep fractures, thermo-hydro-mechanical modeling, 3D

ABSTRACT

The Geothermal Research Initiative (GRI) a group of university, CSIRO and Geoscience Australia researchers have agreed to collaborate on the research and development of geothermal energy resources across a broad range of technologies and geographical locations in Australia. This paper describes the work of a subgroup dedicated to developing a Reservoir Engineering Program specifically designed for extracting heat from the high stress and high temperature structures encountered in Australian conditions. The program was specifically designed to incorporate the insights gained from the failure of the commercial exploitation and the conventional stimulation techniques employed in EGS targets in Australia. The outcomes emphasize the necessity to understand the geological structure providing the pathways for deep fluids.

The current paper explores the use of an innovative 3D numerical technique to characterize these pre-existing geological structures in the context of high temperature deformation and fracture mechanical behavior. Next a stimulation technique for effective stimulation of these pre-existing fractures in the light of the material laws derived in the previous step is presented. This numerically assisted reservoir engineering program has been tested and compared with field observations and laboratory analyses of source rocks under similar tectonic, fluid pressure, chemistry and thermal conditions reproduced in the laboratory. The consideration of previously ignored high temperature deformation mechanisms is expected to provide new unexplored opportunities for the stimulation strategy of EGS plays.

The validated numerical reservoir program is then used to evaluate geothermal energy potential of a typical Australian deep hot crystalline basement in Central Australia. Results of this study include subsurface fracture maps, injection pressure for different flow rates, produced fluid temperature for different circulation periods and flow rates, matrix temperature drawdown and finally the thermal energy recovery factor for different flow rates and production periods.

1. INTRODUCTION

A significant proportion of world’s geothermal systems in particular Australian geothermal reservoirs are characterized by high *in situ* stresses, poorly interconnected fracture systems, large thermal gradients and lack of aquifer support for natural recharge (Narayan et al. 1998) which lead to high impedance between injector and producer wells, thus making them commercially unviable. In order to overcome fluid flow barrier, a combination of hydraulic, thermal and chemical stimulation has to be employed to open, extend and interconnect the pre-existing natural network of fractures to enhance fracture conductivity (Gholizadeh Doonechaly et al. 2012). The potential of the specific subsurface rock masses for construction of a geothermal power plant depends on a number of factors, such as rock type, rock permeability, fracture distribution, subsurface stress field, etc. Rock matrix in Enhanced Geothermal Systems (EGS) has a low permeability. Hydraulic stimulation has been used to reopen existing fracture system and/ or create interconnected fracture system by slip open.(McClure and Horne 2014). Fracture apertures in natural rocks are affected by changes in the effective normal stress and/ or shear displacement (sliding) at the fracture surface. Due to the roughness of the fracture surfaces, the fracture lateral offset causes fracture dilation. Fracture begins to slip when the shear stress acting parallel to the fracture plane exceeds its sliding resistance (Goodman 1976, Willis-Richards et al. 1996). The increase in fracture aperture due to the lateral offset of fracture is an important phenomenon that greatly affects the permeability of the rock masses (Fomin et al. 2003). Several attempts have been made in the past to characterize the shear dilation of the fracture surfaces (Hossain et al. 2002, Rahman et al. 2002). One of the most comprehensive attempts to characterize the shear dilation caused by the fracture surface asperities was developed by Barton et al. (1985). In this model, the rock behavior is described by characteristic properties of fracture surfaces, fracture aperture and the effect of normal and shear displacement on fracture aperture. Main advantages of the model proposed by Barton et al. (1985) are: sample size, laboratory procedure representing fracture surface roughness and coupling between the shear stress, displacement, dilation and conductivity. The main problem in implementing this model, however, is the under-estimation of the hydraulic aperture (Buzzi et al. 2007). Following Barton et al. (1985), Piggott and Elsworth (1991) proposed a methodology based on fracture surface topography to estimate shear displacement under different stresses. Such a topographical model uses empirical correlations to describe the fracture surface roughness both qualitatively and quantitatively. Fracture surface roughness is also characterized by using the self-affine fractal model (Voss 1985, Rayner 1995). Olsson and Brown (1993) developed an experimental procedure to study the effect of normal stress and shear dilation on fluid flow properties of a naturally fractured core sample. They have used a servo-controlled axial/torsion load frame to test the fluid flow and mechanical behavior of the fracture surface under normal stress, slip and shear dilation (Berry et al. 1996). Willis-Richards et al. (1996) proposed an improved methodology to determine the change in fracture aperture based on the amount of shear displacement between the fracture surfaces and the stress boundary condition. They have used the hyperbolic joint closure model to describe the normal compliance of the fractures (Lockner et al. 1977, Hast 1979). Also the effect of fluid pressure on the fracture surface separations is characterized by using normal fracture stiffness. Hossain et al. (2002) and Rahman et al. (2002) extended the work of

Willis-Richards et al. (1996) by considering the effect of fracture propagation during shear dilation event. They used an analytical approach (Rahman et al. 2000) to incorporate the fracture propagation into the modeling procedure.

As mentioned, all the previous attempts focused on fractures with limited sizes subject to uniform stress boundary conditions. It is, however, important to consider fractures subject to varying boundary conditions, such as stress and rock mechanical properties along the surface of the fracture. This can yield a more accurate estimation of the aperture distribution. In this study, an analytical methodology based on distributed dislocation technique proposed by Kotousov et al (2011) is used to estimate the aperture distribution caused by the shear dilation in a fracture subject to varying stress boundary conditions.

The first step in understanding the complex poro-thermo-elastic effects of injected fluid pressure in fractures is the acquisition of characteristic properties of the subsurface fracture system. Numerous methodologies of characterising subsurface fractures have been reported in the literature (Nima). These methodologies are associated with high uncertainties due to lack of verification. In order to reduce the uncertainty we used a two steps procedure: first, tracking the fracture backbone in microseismic cloud events is used to generate a subsurface map. Then the numerical model for simulation of pressure derivatives was validated against an analytical solution. The authors selected Habanero enhance geothermal reservoir to study the effect of induced fluid pressure on the change of fracture aperture and consequent change in permeability. In order to verify the numerical model it is used to simulate pressure derivatives and then compared the pressure derivatives with that from pressure drawdown data.

Following verification of subsurface fracture map the reservoir is subjected to injected fluid pressure. The pressurization is performed by injecting fluid through Habanero #1 while keeping Habanero #2 and Habanero #3 closed. Well location and distance between wells are chosen based on the Habanero geothermal system.

Despite the presence of multiple fractures in various sections of the Habanero geothermal reservoir, the vast majority of fluid flow occurs over a short section of intensely fractured zone referred to as the “Main Fracture” (Bendall et al.). An analysis of hot water production is performed for three well configurations, Habanero #1 is the injection well and Habanero well #2 & #3 are the production wells.

2 METHODOLOGY

In this study, a comprehensive numerical methodology is proposed to (a) generate the subsurface fracture map of the reservoir, (b) simulate fluid flow and heat transfer as a result of cold fluid injection and (c) evaluation of the shear dilation events within the reservoir to estimate the reservoir stimulation. The proposed methodology is explained in details as follows.

2.1 Generation of Subsurface Fracture Map

Seismic surveys are widely utilized to understand the subsurface fracture map of the reservoirs (Gholizadeh Doonechaly and Rahman 2012). Microseismic events recorded during water injection occur primarily at the tips of the fractures (Warpinski et al. 2004). Assuming that all the recorded events are tip-events, a fracture network backbone may be computed using a Euclidean Minimum Spanning Tree (EMST) algorithm (March et al. 2010). Figure 1 show the complete Fracture Network generated in this study by using EMST in a plan view. Details of this fracture network are shown in figures 2 and 3. Figure 4 shows the same network detail as Figure 3 with the addition of the location of the microseismic events colored using their recorded magnitude.

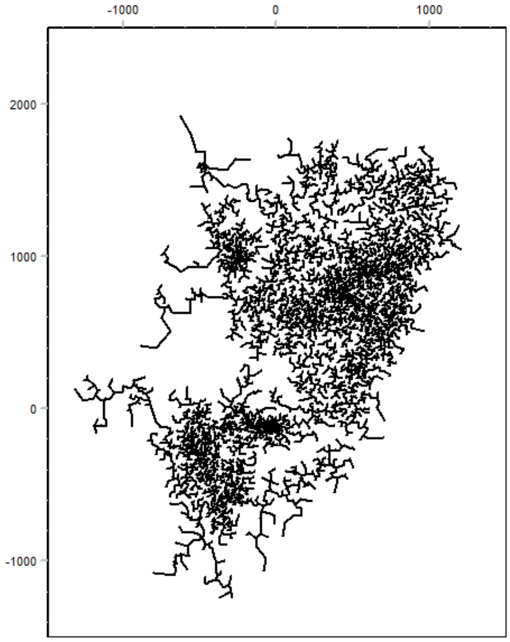

Figure 1: Complete fracture network for the Habanero field generated in this study by the EMST algorithm

To estimate the fracture planes the length of each segment in the fracture network backbone was computed and a fracture height was assigned based on a height to length ratio. The initial value of this ratio was set to be 0.1, though this is a parameter that can be adjusted. Dip angles for the fractures were assigned stochastically based upon the mean and variance of dip-angle distributions measured in similar environments from image logs. This process creates a complete 3D backbone of the fracture network linking each of the microseismic events.

The assumption that all microseismic events that are recorded during pumping occur at the tips of the existing fracture network is not necessarily correct. Figure 5 shows the microseismic events recorded at the Habanero site up to and including 12 September 2005. There are clearly multiple clusters of data. The events in the south west are those associated with pumping in Habanero #2 which commenced on 7 August 2005. The large cluster in the north east is associated with pumping in Habanero #1 which started on 6 September but stopped for 48 hours on September 8 due to a pump malfunction. A time-stepped EMST algorithm is being developed to add events to an existing EMST which would result in a more accurate fracture backbone. Figure 5 shows more than two clusters of events. There are individual events between the two well-induced clusters, and there is another cluster between the two wells. These individual points and the smaller cluster between the two wells could be due to extension of the existing fracture network from Habanero #1 or Habanero #2, or it could be induced seismicity due to the changing stress conditions resulting from pumping into the two wells. The fracture network that is created would be different for these two different alternatives, and a scenario-based algorithm for the computation of an accurate fracture network backbone is currently being developed. This algorithm uses additional information from the microseismic signatures to classify microseismic events as a pre-processing step to the construction of the EMST.

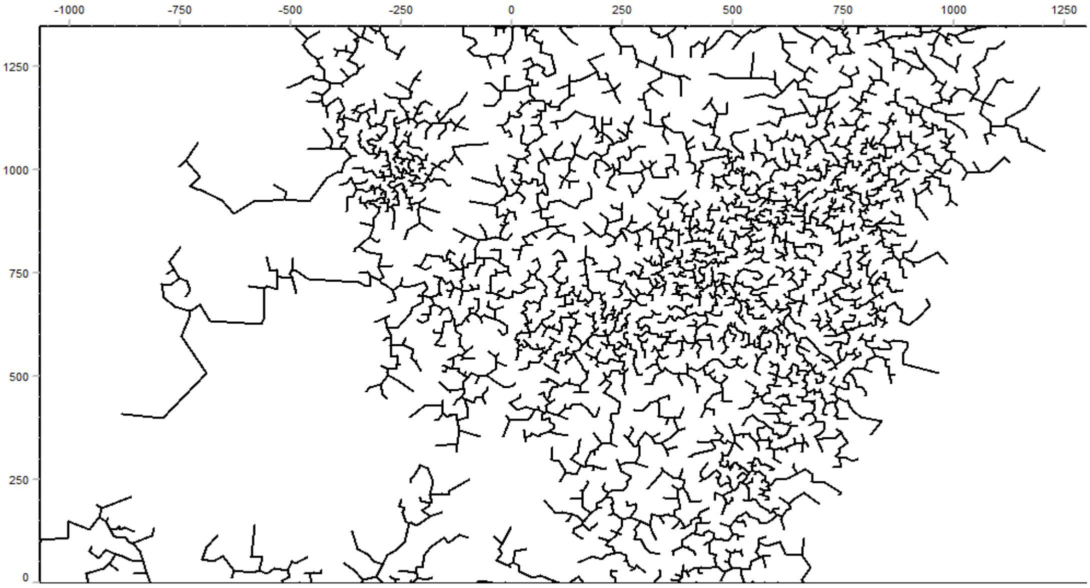

Figure 2: Fracture network detail for the Habanero field generated in this study by the EMST algorithm

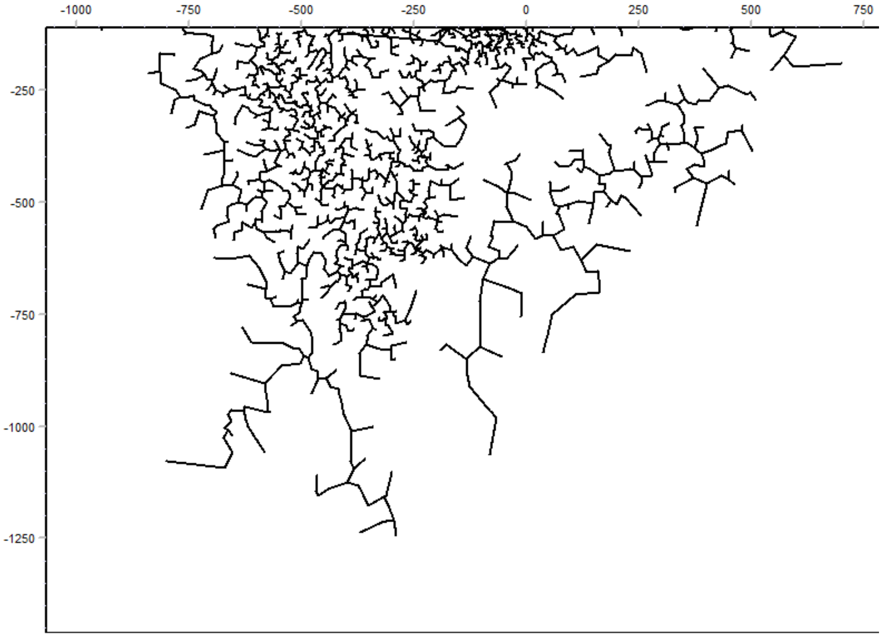

Figure 3: Fracture network detail of the lower part of the Habanero field generated by EMST algorithm.

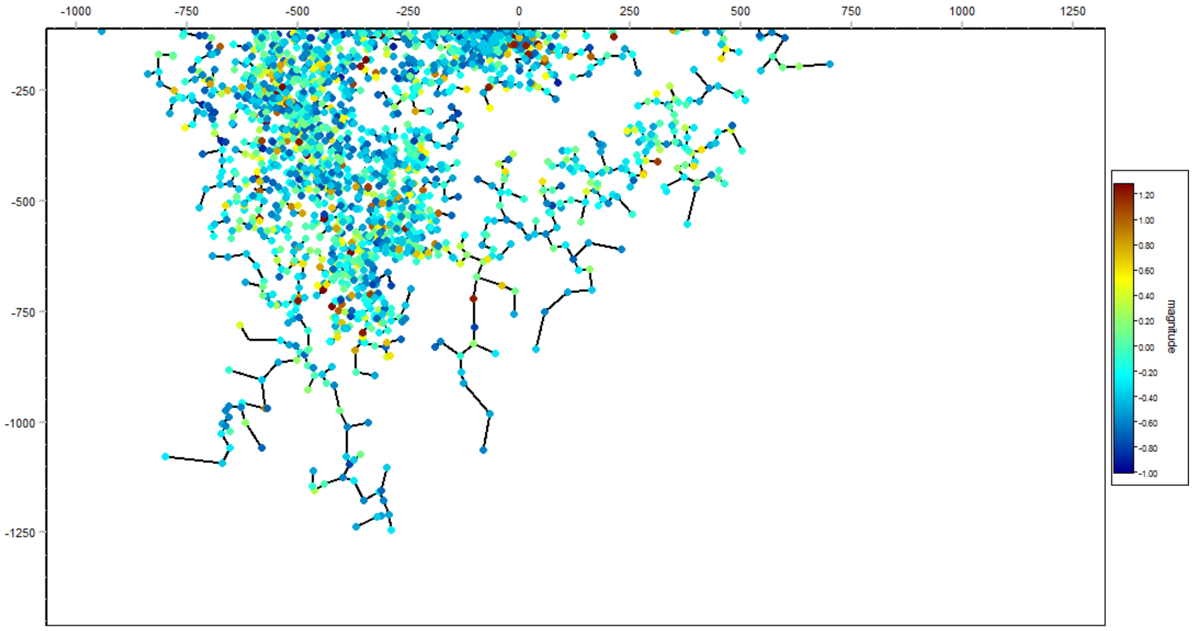

Figure 4: Fracture network detail showing event magnitude for the lower part of the Habanero geothermal field.

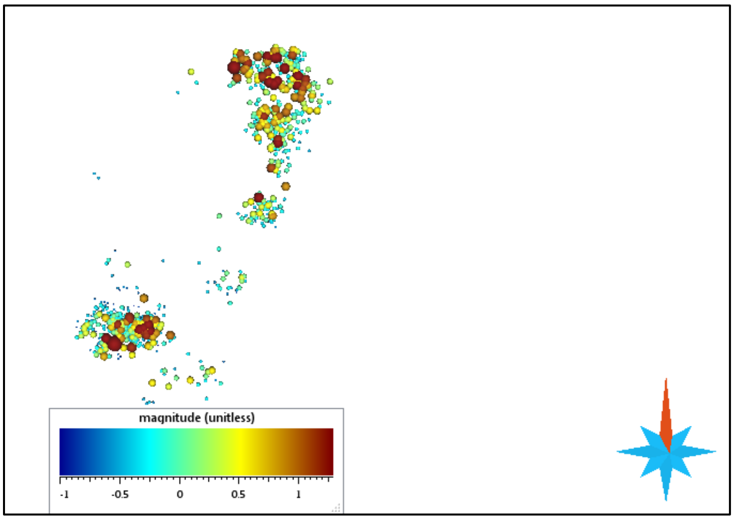

Figure 5: Microseismic events recorded until to 12 September 2005.

2.2 Poro-thermo-elastic Simulation

In this study the small fractures ($l < 20$m) are considered as part of matrix porosity. First the reservoir domain is discretised along with medium to long fractures ($l>20$m) using tetrahedral elements of different size and geometry. Different tetrahedral elements have allowed us to refine mesh along the medium to large fractures. Next, permeability tensor of each tetrahedral element was determined using finite element technique (see Appendix A for the full methodology and description). Finally, finite element technique is employed to simulate fluid flow and rock deformation in reservoir domain. In order to discretise the mass-, momentum- and energy-conservation equations, the weighted residual method and the Green's theorem are applied (Bathe 1996). The finite-element method is used in this study for the purpose of numerical simulation purpose. Therefore the state variables (namely: displacement, pore pressure and temperature) are defined using proper shape functions as:

$$u = N_u \overline{u} \tag{1}$$

$$p = N_p \overline{p} \tag{2}$$

$$T = N_T \overline{T} \tag{3}$$

where, N is the corresponding shape function and $\overline{u}$, $\overline{p}$ and $\overline{T}$ are the nodal values of the corresponding state variable. By applying the Galerkin's method and replacing the weighting functions by the corresponding variables' shape functions, the weak form of the conservation equations can be written as follows (Watanabe et al. 2010, Watanabe 2012):

$$\int_{\Omega} wS_s \frac{\partial p}{\partial t} d\Omega + \int_{\Omega} w^T \alpha \nabla \cdot \frac{\partial u}{\partial t} d\Omega + \int_{\Omega} w\beta \frac{\partial T}{\partial t} - \int_{\Omega} \nabla w^T \cdot q_H d\Omega + \int_{\Gamma_H^q} w(q_H \cdot n) d\Gamma - \int_{\Omega} wQ_H d\Omega = 0 \tag{4}$$

$$\int_{\Gamma_d} wb_m S_s \frac{\partial p}{\partial t} d\Gamma + \int_{\Gamma_d} w\alpha \frac{\partial b_m}{\partial t} d\Gamma + \int_{\Gamma_d} w\beta \frac{\partial T}{\partial t} d\Gamma - \int_{\Gamma_d} \nabla w^T \cdot (b_h q_H) d\Omega + \int_{\Gamma_H^q} wb_h (q_H \cdot n) d\Gamma + \int_{\Gamma_d} wq_H^+ d\Gamma + \int_{\Gamma_d} wq_H^- d\Gamma = 0 \tag{5}$$

$$\int_{\Omega} wc_p \rho \frac{\partial T}{\partial t} d\Omega + \int_{\Omega} wc_p \rho q_H \cdot \nabla T d\Omega - \int_{\Omega} \nabla w^T \cdot (-\lambda \nabla T) d\Omega + \int_{\Gamma_T^q} w(-\lambda \nabla T \cdot n) d\Gamma - \int_{\Omega} w^T Q_T d\Omega = 0 \tag{6}$$

$$\int_{\Gamma_d} wb_m c_p^l \rho^l \frac{\partial T}{\partial t} d\Gamma + \int_{\Gamma_d} wc_p^l \rho^l b_h q_H \cdot \nabla T d\Gamma - \int_{\Gamma_d} \nabla w^T \cdot (-b_m \lambda^l \nabla T) d\Gamma + \int_{\Gamma_T^q} w(-b_m \lambda^l \nabla T \cdot n) d\Gamma + \int_{\Gamma_d} wq_T^+ d\Gamma + \int_{\Gamma_d} q_T^- d\Gamma = 0 \tag{7}$$

$$\int_{\Omega} \nabla^s w^T \cdot (\sigma' - \alpha pI) d\Omega - \int_{\Omega} w^T \cdot \rho g d\Omega - \int_{\Gamma_t} w^T \cdot \bar{t} d\Gamma - \int_{\Gamma_d} w^{+T} \cdot t_d^+ d\Gamma - \int w^{-T} \cdot t_d^- d\Gamma = 0 \tag{8}$$

where w is the test function, Ω is the model domain, Γ is the domain boundary, t is the traction vector and d is the fracture plane.

2.3 Validation of Numerical Fluid Flow Model

To validate the numerical model, a sugar-cube reservoir has been created using an in-house 3D mesh generator code with two set of orthogonal vertical fractures having the same dip angle and different azimuth. An equal fracture spacing of 250 m is assumed with a vertical well at the center of the model penetrating the whole reservoir thickness. Horizontal fractures are ignored as they are usually not observed below moderate depth, so only vertical fractures are considered. Properties of the fractures, matrix and stress values are presented in Table (1). A single-phase draw-down test is performed for 3,500 days at a constant production rate of 5,000 bbl/day simulated numerically using a discrete-fracture approach.

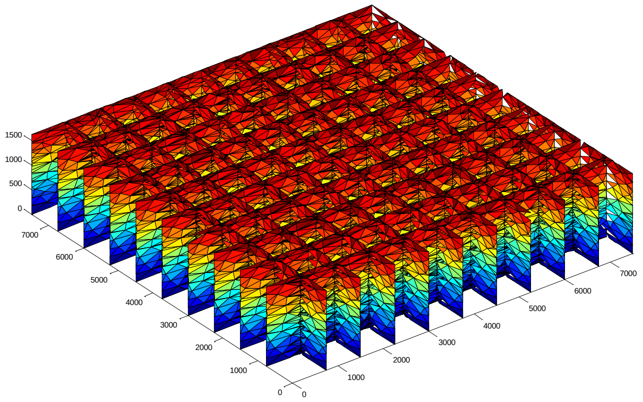

Figure 6: Sugar cube model with a two set of orthogonal vertical fractures and a vertical well penetrating the model from top to the bottom at the centre of the domain.

The pressure response at the wellbore was compared against an analytical pressure-transient solution introduced by (Warren and Root 1963) for dual-porosity model.

Table-1: Input data for the sugar cube model used in the numerical simulation for validation process.

Reservoir dimensions	7500m x 7500m x1620 m
Fracture spacing	250m
Matrix permeability	0.01mD
Matrix porosity	0.01
Fracture permeability	1000mD
Wellbore storage	0 bbl/psi^{-1}
Initial reservoir pressure	10,000psia
Fluid viscosity	0.2cp
Fluid compressibility	22.4E-06psi^{-1}
Horizontal stresses	9000psi
Vertical stress	12000psi

In Figure 7 the simulated and the actual pressure change and pressure derivatives are presented. The pressure derivative curve is like a bell shaped between 20 hrs. to 1000 hrs., indicating a transition flow period. In this flow period the matrix starts to feed the fractures network by fluid. During this period the fluid production at the wellbore is very low and pressure starts to drop slowly. The dip of this bell shaped is controlled by the value of storativity ratio (ω). As the (ω) gets smaller, the dip gets deeper and starts earlier.

The horizontal portion of the pressure derivative curve from 1000 hrs. to 40,000 hrs. indicates the end of transition period and start of the composite system flow. This flow period is controlled by the value of inter-porosity flow coefficient (λ). The unit slope of pressure derivative curve between 10,000 hrs. to 100,000 hrs. indicates pseudo steady-state condition for the entire reservoir volume. By using this flow period, a reservoir volume and shape can be calculated. At early time response for idealized dual porosity transient behavior with a very low wellbore storage effects, a first radial flow regime is expected to appear before starting of transition flow period. This radial flow regime is governed by the flow only inside the fractures. As shown in Figure 7, there is a good agreement between the results of this study with that of the analytical solution.

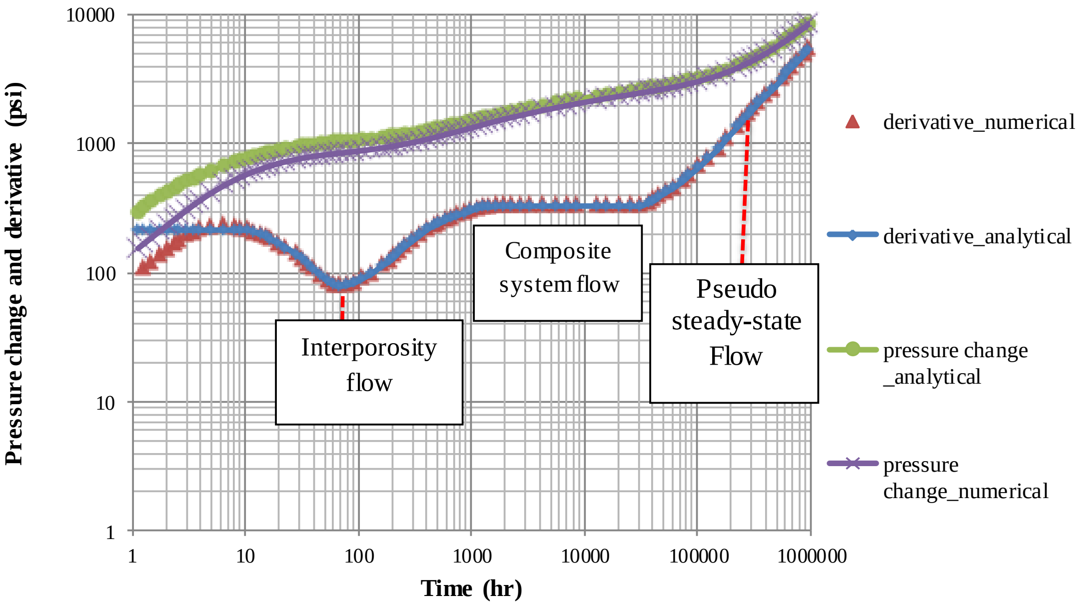

Figure 7: Pressure transient response of the sugar cube model generated by the developed model in the current study against that of generated with the dual porosity model.

2.4 Verification of Subsurface Fracture Map

Pressure drawdown in the production well Habanero #2 versus time and its derivative are presented in Figures 8 and 9 respectively. The results of this study are also compared with that from Habanero geothermal reservoir. As can be seen in Figure 8, the pressure profile from both studies exhibit the same pattern with the exception that, at the early times, the change in pressures are shifted by about half a cycle from that of the measured data. This shift at early times is due to the lack of information on reservoir properties. It is, however, noteworthy that the pressure derivatives obtained based on the current study are in a good agreement with that of the measured data from the Habanero geothermal reservoir.

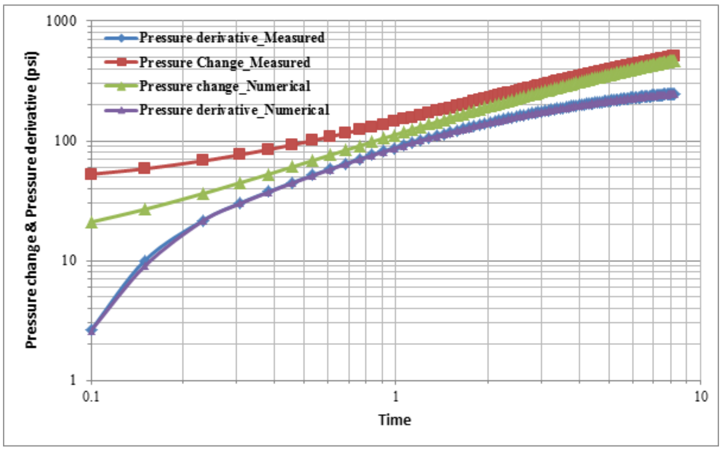

Figure 8: Log-log plot of pressure derivative and pressure change of the draw down test conducted in Habanero #2 well.

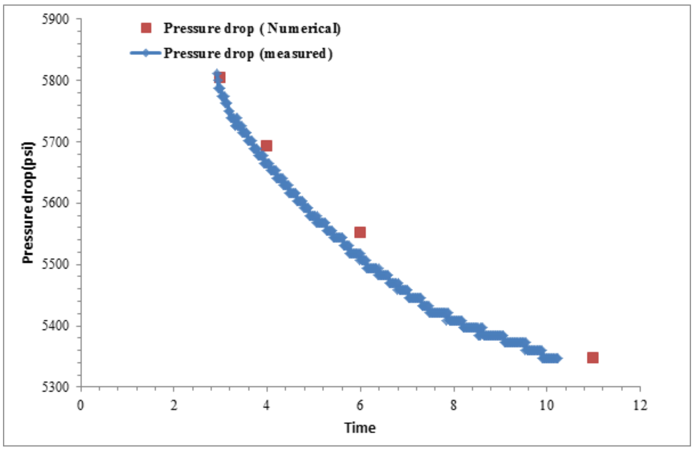

Figure 9: Plot of the drawdown history of Habanero #2.

2.5 Shear Dilation of the Fracture Surfaces

The change in aperture distribution along the fracture surface due to induced fluid pressure is calculated based on an analytical methodology in which fracture geometry, stress distribution and fluid pressure inside the fracture are needed to be known as a priori. For this purpose the developed thermo-poro-elastic model (see above) is used to simulate the fluid flow in the reservoir scale. In current study, an analytical computational methodology based on distributed dislocation technique proposed by Kotousov et al. (2011) is used to estimate the aperture distribution caused by the shear dilation in a fracture subject to different varying stress boundary conditions. Two major assumptions are used in this approach to characterize the shear dilation of the fracture surfaces. The shear slippage between the fracture surfaces is described by using Coulomb friction law which explains the friction stress during the shear slippage based on the normal stress exerted on the fracture planes with a proportionality contact named friction factor as:

$$\tau_n = \tau_0 + f\sigma_n \tag{9}$$

Where, τ_0 is the threshold shear stress value to initiate the shear slippage between the fracture surfaces. Also the friction factor, f, is dependent on the material properties, fracture geometry and surface asperities of the fracture (Kotousov et al. 2011). Estimation of the shear dilation caused by the shear slippage of the fracture surfaces is of crucial importance in many areas especially fluid flow simulation. Because a minor change in the fracture aperture causes a significant alteration of the fracture permeability. In this study the coupling between the shear displacement and the change in fracture aperture is described by via a step function. Fracture displacement normal to the fracture plane is simulated by using virtual springs distributed along the fracture length. Such springs are characterized by a specific spring constant which can be calculated numerically, experimentally or analytically (Kotousov et al. 2011). Also the spring deformations are modeled in an elastic framework which results in the following system of equations describing the stress between the fracture surfaces as:

$$\sigma_n = kE(\Delta - \delta_y) \quad \text{for} \quad \delta_y < \Delta \tag{10}$$

$$\sigma_n = 0 \text{ for } \delta_y > \Delta \tag{11}$$

Where, Δ is the characteristic height of the fracture and k is the spring constant. In this study, the methodology proposed by Gangi (1978) is used to calculate the spring constant based on the proposed bed of nails as:

$$k = E\frac{b\Delta}{L} \tag{12}$$

Where, E is the Young modulus of elasticity, L is the fracture length and b is a constant less than unity.

3. RESULTS AND DISCUSSIONS

The proposed methodology is used to study the pressure response of the Habanero geothermal reservoir during the injection of the cold fluid (Bendall et al. 2014). The pressurization of the reservoir is carried out over a period of 12 days. During this period, the reservoir is pressurized and the change in fracture aperture monitored. Following the stimulation of the reservoir a flow test is also carried to evaluate the potential of hot water production from Habanero reservoir. The results of change in average fracture aperture within the reservoir against the stimulation time are presented in Figure 10. After 300 hours (12.5 days) of stimulation an average increase in aperture by 20% is observed. It is also observed that the rate of increase in aperture is near linear. In Figure 11 the pressure profile after 40hrs (left) and 100hrs (right) of injection are presented. In Figure 12 the pressure drop between the injection and production wells as a function of production rate is presented. Pressure drop can be perceived as the energy spent to overcome the reservoir impedance. This means that, initially, production rate increases as more energy spent to overcome the reservoir impedance. This increase in production, however, levels out at about 50l/s for an impedance of 6000psi. Any further increase in pressure drop (spent energy) does not increase production rate significantly. This suggest that an optimum injection rate can be obtained for a given stimulation pressure.

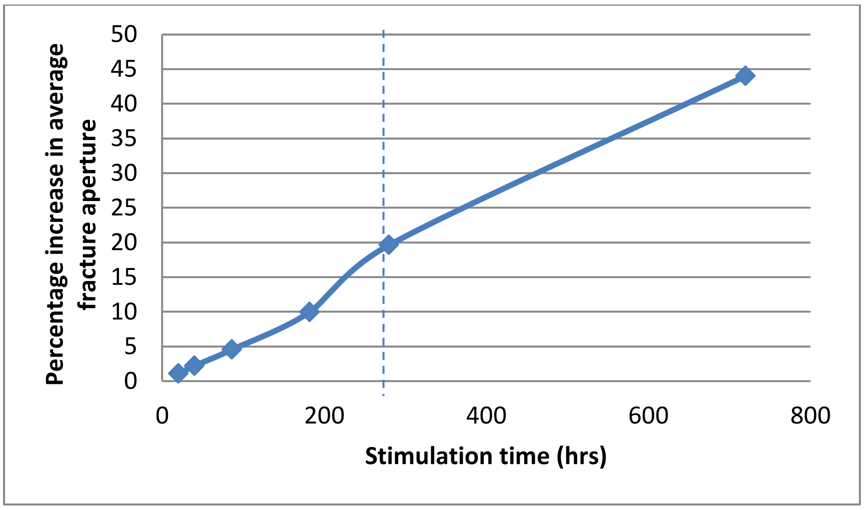

Figure 10: Average increase in fracture apertures versus time due to injected fluid pressure of 51.1MPa; σ_H = 62 MPa, σ_h = 58.6 MPa and σ_v = 82.7 MPa.

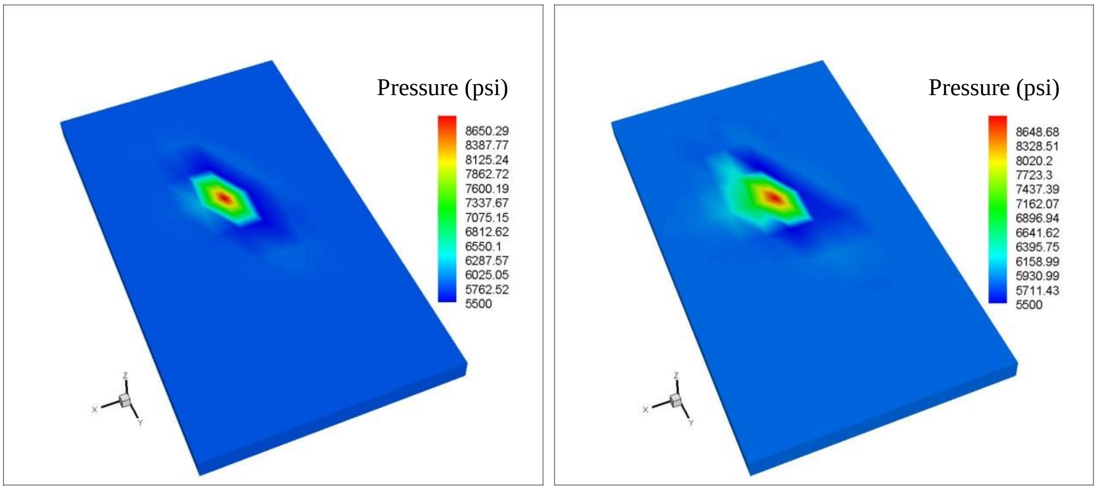

Figure 11: Pressure distribution after 40hrs (left) and 100hrs (right) of injection of fluid at 51.1MPa; σ_H = 62 MPa, σ_h = 58.6 MPa and σ_v = 82.7 MPa.

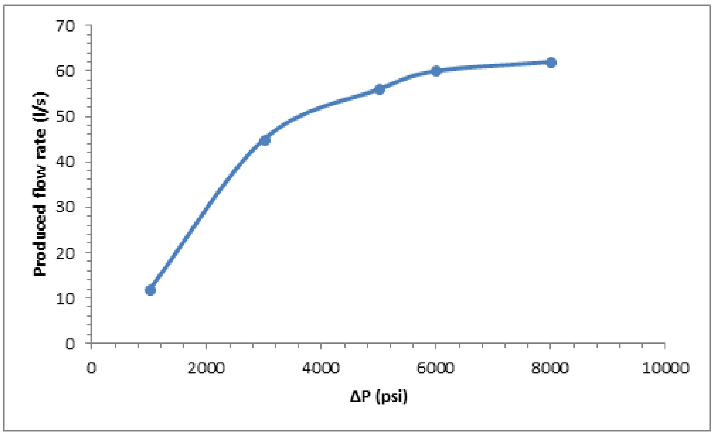

Figure 12: Reservoir impedance at different production rate; σ_H = 62 MPa, σ_h = 58.6MPa and σ_v = 82.7 MPa.

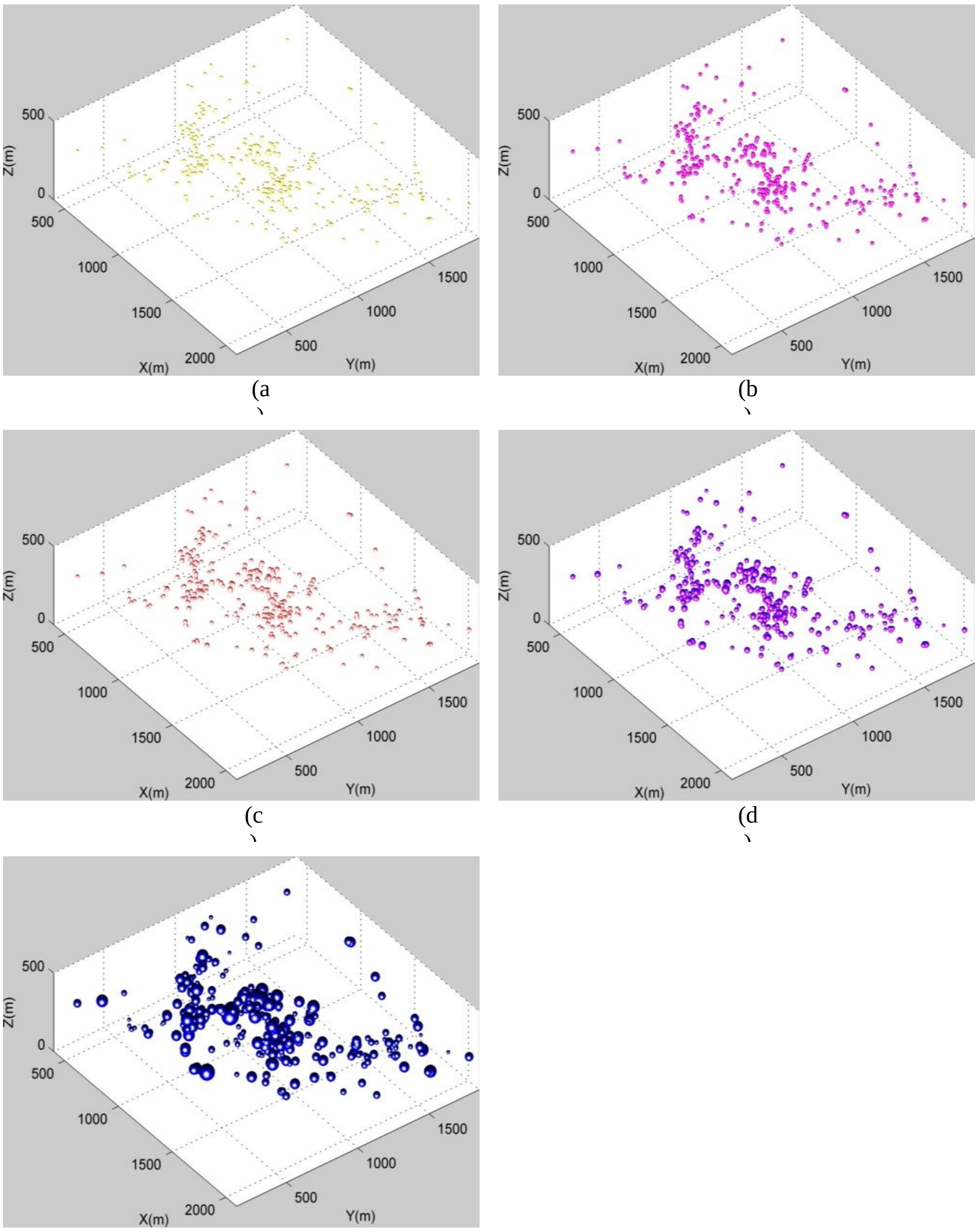

(a)

(b)

(c)

(d)

(e)

Figure 13: Location and size of the dilation events due to the injected fluid pressure of 51.1MPa, σ_H = 62 MPa, σ_h = 58.6 MPa, σ_v = 82.7 MPa, Ti = 250°C, after (a) 20hrs, (b) 100hrs, (c) 96hrs, (d) 288hrs and (e) 720hrs. (The radiuses of the spheres are not in scale).

The location and magnitude of the shear dilation events are also presented in Figure 13. As shown in the Figure 13, during the injection period (720hrs) there has been significant increase in shear dilation, however, the magnitude of dilation (increase in aperture) increases with time. Noteworthy, the increase in dilation magnitude remain small until 12 days (288hrs) of stimulation after which a significant increase in the dilation event (size of the spheres) can be observed. The stimulation results also show that the dilation events grow horizontally in all directions. The Habanero stimulation field test for a period of 12 days showed a downward as well as horizontal propagation of the dilation events. It has been postulated that downward propagation of dilation events is due to existence of fracture network which stems from longer time-scale processes (known as thermally activated creep processes) than previously thought (Fusseis et al. 2009, Lieb et al. 2012). Although the current study does not consider thermally activated creep process over longer term results show that new techniques has the potential to improve our understanding of stimulation behavior when subjected to induced fluid pressure. A comparative study of the location of the microseismic events produced during field test at Habanero geothermal reservoir and the current numerical study is made and presented in Figure 14. The blue circles represent events generated due to injection of fluid after 30 days and the green circles present the location of the dilation events observed based on the current study. Results of this study show a close match with that from the field test.

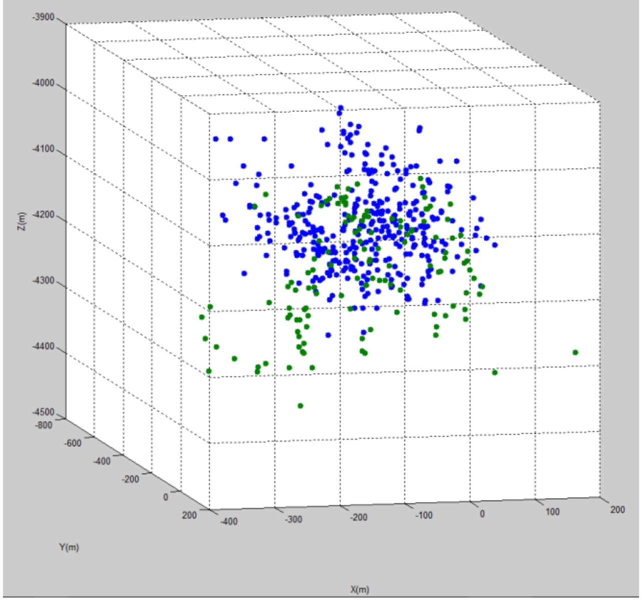

Figure 14: A comparison between the dilation events in this study (green circles) with that from the field test trial (blue circles) with σ_H = 62 MPa, σ_h = 58.6MPa, σ_v = 82.7 MPa, Pinj = 49.6 MPa and P_i = 35.16 MPa after 30 days of fluid injection.

Following the stimulation a numerical experiment is carried out to evaluate the produced fluid temperature as a result of the cold fluid circulation over a production period of 12 years. The results of this experiment are presented in Figures 15-18. Figure 15 shows the reservoir pressure profile after 1 (left) year and after 6 (right) years of cold fluid circulation. As shown by the figure, after one year of production, fluid only swept through the long interconnected fracture system. However, after six years of production the injection pressure significantly advanced towards the production well. At this stage, the fluid swept through the major parts of the reservoir.

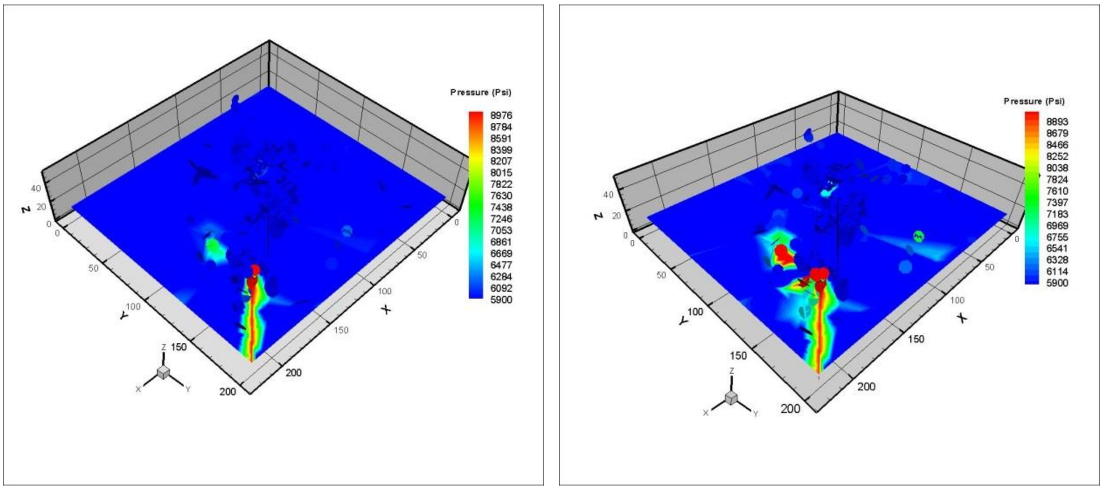

Figure 15: Reservoir pressure profile in Habanero reservoir with σ_H = 62 MPa, σ_h = 58.6MPa, σ_v = 82.7 MPa, Pinj = 49.6 MPa, Δp = 21.37 MPa, Tinj = 100°C, Ti = 250°C and P_i = 35.16 MPa after 1 year (left) and 6 years (right). Long fractures which are used for the discrete fracture mesh generation are presented in the figure.

Figure 16 presents the matrix temperature altered by the cold fluid circulation. As shown in Figure 16 (top) after one year of circulation the temperature of a small part of the reservoir is affected. After six years of circulation (Figure 16 (bottom)), however, the fluid sweeps over a larger part of the reservoir which increases the thermal drawdown. Figure 17 presents the produced fluid temperature as a function of time. As shown in the figure, the produced fluid temperature remains constant at the beginning of the hot water production. From Figure 17, it can also be observed that the thermal breakthrough occurs after two years of cold fluid circulation after which the produced fluid temperature starts to decrease. With the time, the rate of thermal drawdown increases. This is attributed to the fact that thermal draw down causes additional thermal stresses which further increase the fracture apertures. In another word, thermal stresses contribute to development of new flow paths and, therefore increase the effective volume of the reservoir. Simulated thermal stress profile of the Habanero geothermal reservoir after 6 years of cold fluid circulation is presented in Figure 18. As shown in the figure the thermal stresses significantly grow throughout the reservoir after six years of cold fluid circulation which in turn reduces the effective stress in the corresponding regions significantly.

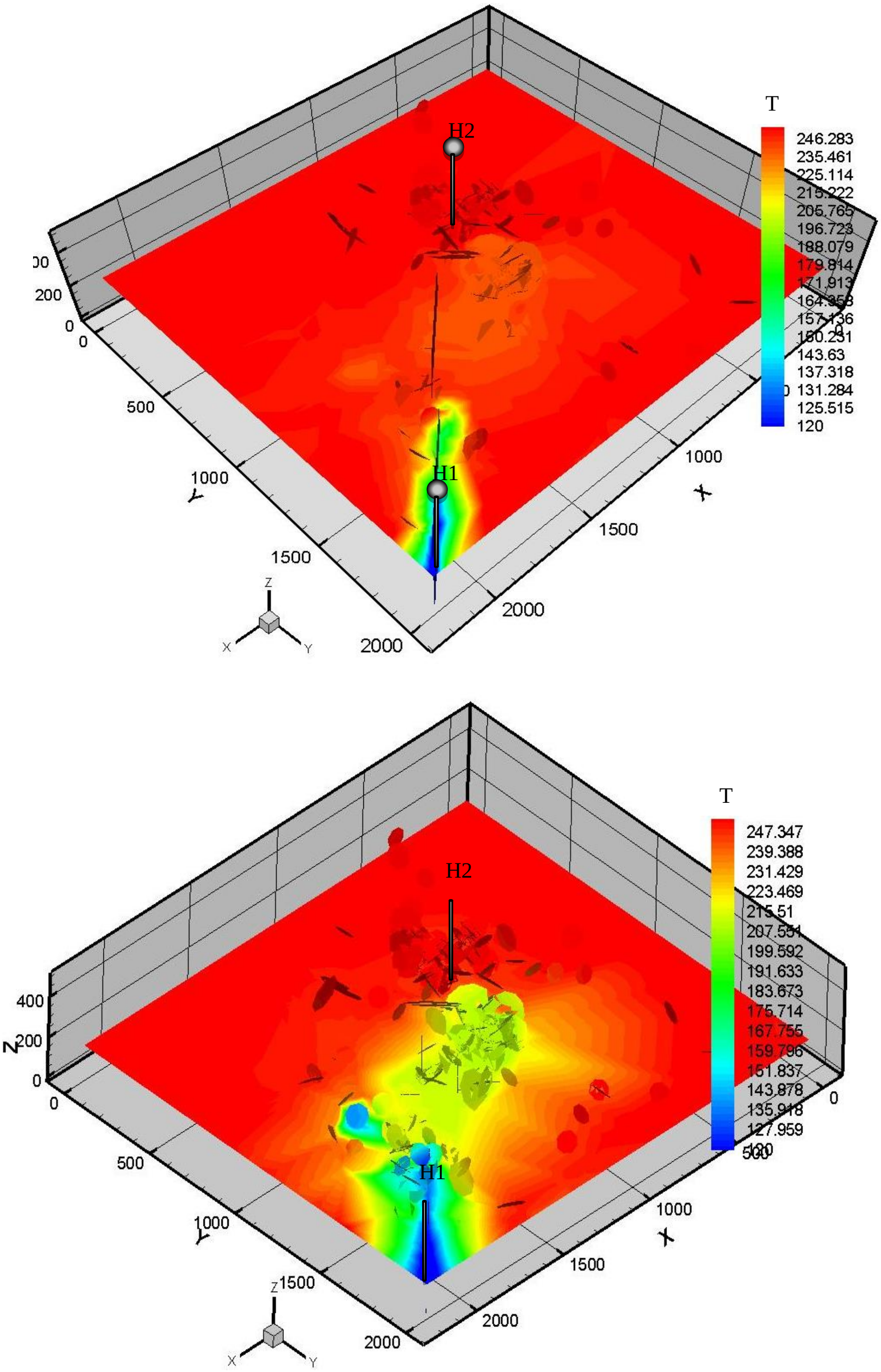

Figure 16: Rock matrix temperature distribution in °C in Habanero reservoir with σ_H = 62 MPa, σ_h = 58.6MPa, σ_v = 82.7 MPa, Pinj = 49.6 MPa, Δp = 21.37 MPa, Tinj = 100°C, Ti = 250°C and P_i = 35.16 MPa after 1 year (top) and 6 years (bottom). Long fractures which are used for the discrete fracture mesh generation are presented in the figure.

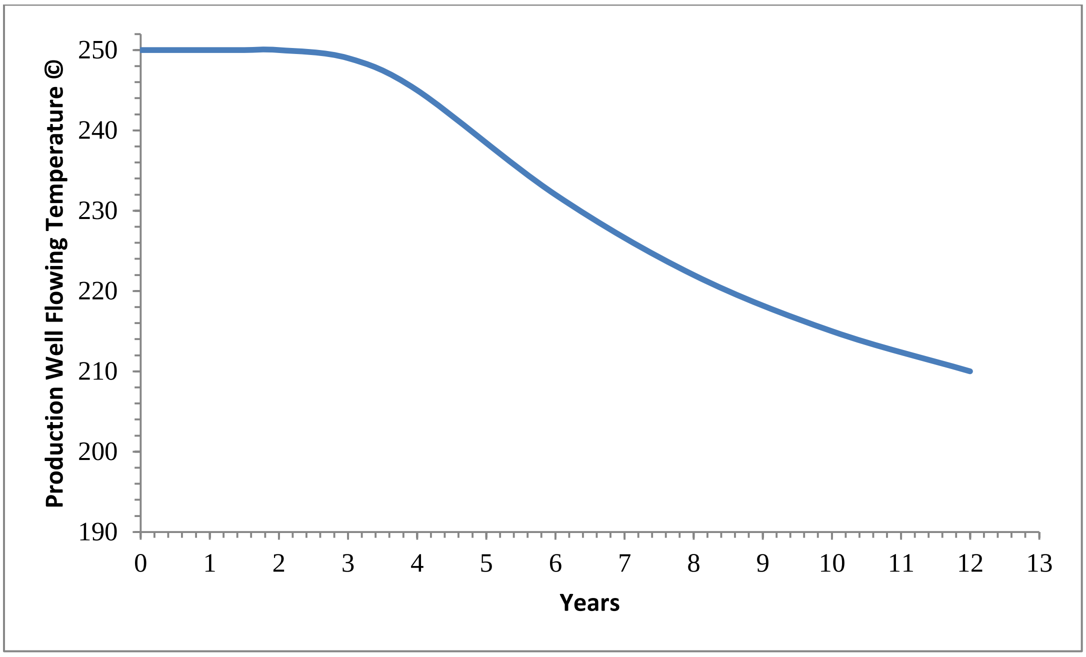

Figure 17: Produced fluid temperature as a function circulation time (for a period of 12 years); σ_H = 62 MPa, σ_h = 58.6MPa, σ_v = 82.7 MPa, Tinj = 100°C, Ti = 250°C, the injector bottomhole pressure, Pinj is kept constant at 48.95 MPa, with an injector–producer pressure impedance (Δp) of 21.37 MPa and initial reservoir pressure of P_i = 35.16 MPa.

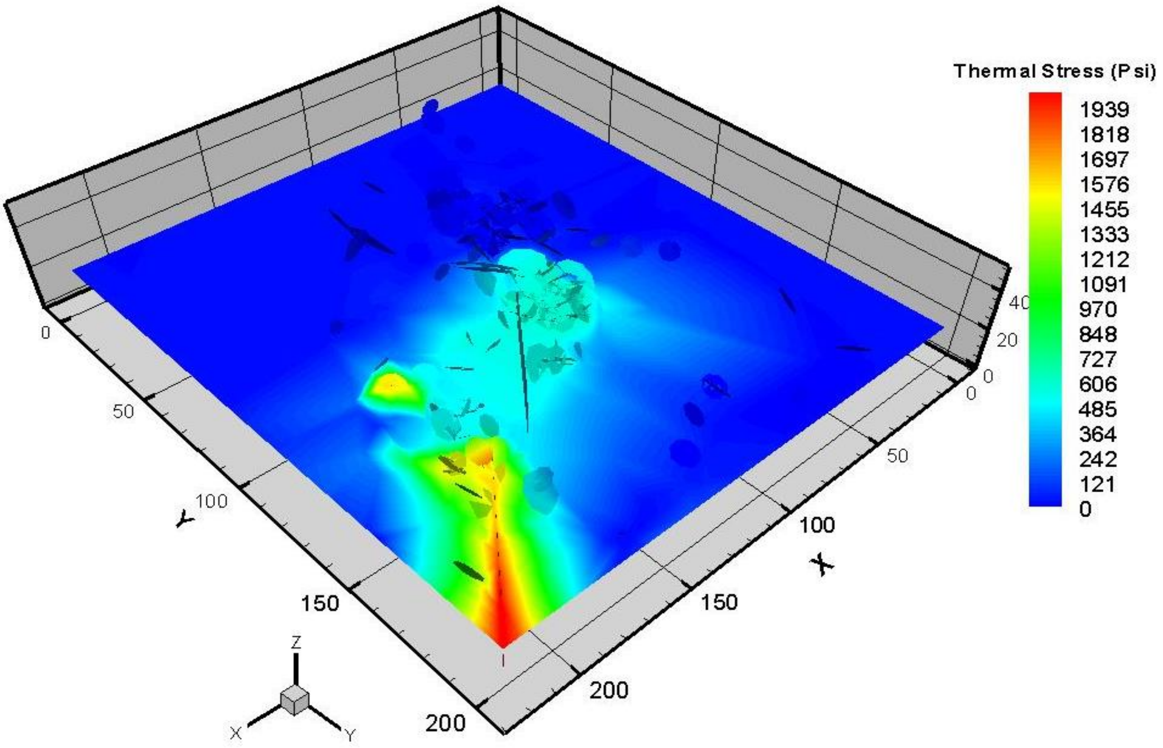

Figure 18: Thermal stresses after 6 years of cold fluid circulation. Cold water injected at Tinj = 100°C. Initial reservoir temperature Ti = 250°C and initial reservoir pressure P_i = 35.16 MPa, σ_H = 62 MPa, σ_h = 58.6MPa and σ_v = 82.7 MPa.

CONCLUSIONS

In this paper an innovative methodology is proposed to evaluate the stimulation of an Australian geothermal reservoir in a numerical thermo-poro-elastic framework. A semi-analytical approach is used to evaluate the change in fracture aperture at different stress and fluid pressure condition. The results of the developed technique were applied to the Habanero geothermal reservoir in Australia and the results were compared with that of the field measurements. The numerical results show that the dilation events propagate horizontally. Results of matrix drawdown and produced fluid temperature show rapid thermal draw down of the reservoir after the thermal breakthrough. This is due to the fact that a few numbers of interconnected fractures are taking part in fluid circulation between injection and production wells which causes rapid cooling of the matrix. Another critical observation is that the effective stresses decrease as matrix cools down due to the fluid circulation as a result of thermal stresses. This, in turn, helps to increase fracture permeability and reduce impedance fluid circulation.

ACLNOWLEDGEMENT

The authors would like to thank the Geodynamics Limited for providing valuable data for this study.

REFERENCES

Barton, N., S. Bandis and K. Bakhtar (1985). "Strength, deformation and conductivity coupling of rock joints." International Journal of Rock Mechanics and Mining Sciences & Geomechanics Abstracts **22**(3): 121-140.

Bathe, K. J. (1996). Finite element procedures, Prentice Hall.

Bendall, B., R. Hogarth, H. Holl, A. McMahon, A. Larking and P. Reid "Australian Experiences in EGS Permeability Enhancement–A Review of 3 Case Studies."

Bendall, B., R. Hogarth, H. Holl, A. McMahon, A. Larking and P. Reid (2014). "Australian Experiences in EGS Permeability Enhancement–A Review of 3 Case Studies."

Berry, M. D., D. W. Stearns and M. Friedman (1996). "The Development of a Fractured Reservoir Model for the Palm Valley Gas Field." Journal of the Australian Petroleum Production and Exploration Association Ltd: 82-103.

Buzzi, O., J. Hans, M. Boulon, F. Deleruyelle and F. Besnus (2007). "Hydromechanical study of rock–mortar interfaces." Physics and Chemistry of the Earth, Parts A/B/C **32**(8–14): 820-831.

Fomin, S., A. Shimizu, K. Matsuki, K. Sakaguchi and T. Hashida (2003). Simulation of the fracture shear dilation. Sixth International Workshop on Nondestructive Testing and Computer Simulations in Science and Engineering, International Society for Optics and Photonics.

Fusseis, F., K. Regenauer-Lieb, J. Liu, R. M. Hough and F. De Carlo (2009). "Creep cavitation can establish a dynamic granular fluid pump in ductile shear zones." Nature **459**(7249): 974-977.

Gangi, A. F. (1978). "Variation of whole and fractured porous rock permeability with confining pressure." International Journal of Rock Mechanics and Mining Sciences & Geomechanics Abstracts **15**(5): 249-257.

Gholizadeh Doonechaly, N. and S. S. Rahman (2012). "3D hybrid tectono-stochastic modeling of naturally fractured reservoir: Application of finite element method and stochastic simulation technique." Tectonophysics **541–543**(0): 43-56.

Gholizadeh Doonechaly, N., S. S. Rahman and A. Kotousov (2012). "A Realistic Assessment of Recoverable Thermal Energy from Australian Geothermal Reservoirs: A Simulation Study." Proceedings of the 2012 Australian Geothermal Energy Conference

Goodman, R. E. (1976). Methods of geological engineering in discontinuous rocks.

Hast, N. (1979). "Limits of stress measurements in the Earth's crust." Rock mechanics **11**(3): 143-150.

Hossain, M. M., M. Rahman and S. Rahman (2002). "A shear dilation stimulation model for production enhancement from naturally fractured reservoirs." Spe Journal **7**(2): 183-195.

Hossain, M. M., M. K. Rahman and S. S. Rahman (2002). "A Shear Dilation Stimulation Model for Production Enhancement From Naturally Fractured Reservoirs." SPE Journal **7**(2): 183-195.

Kotousov, A., L. Bortolan Neto and S. Rahman (2011). "Theoretical model for roughness induced opening of cracks subjected to compression and shear loading." International Journal of Fracture **172**(1): 9-18.

Lieb, K. R., R. Jeffrey, S. Rahman, M. Trefry, A. Karrech, A. Bunger, A. Dyskin, X. Zhang, B. Wu and M. Veveakis (2012). "Deep Geothermal: A Science Proposition."

Lockner, D. A., J. B. Walsh and J. D. Byerlee (1977). "Changes in seismic velocity and attenuation during deformation of granite." Journal of Geophysical Research **82**(33): 5374-5378.

March, W. B., P. Ram and A. G. Gray (2010). Fast euclidean minimum spanning tree: algorithm, analysis, and applications. Proceedings of the 16th ACM SIGKDD international conference on Knowledge discovery and data mining, ACM.

McClure, M. and R. Horne (2014). "Characterizing Hydraulic Fracturing With a Tendency-for-Shear-Stimulation Test." SPE Reservoir Evaluation & Engineering(Preprint).

Narayan, S. P., Z. Yang, S. S. Rahman and Z. Jing (1998). "Propant Free-Shear Dilation: An Emerging Techology for Exploiting Tight to Ultra-Tight Gas Resources." SPE Annual Technical Conference and Exhibition, 27-30 September 1998, New Orleans, Louisiana.

Olsson, W. A. and S. R. Brown (1993). "Hydromechanical response of a fracture undergoing compression and shear." International Journal of Rock Mechanics and Mining Sciences & Geomechanics Abstracts **30**(7): 845-851.

Piggott, A. R. and D. Elsworth (1991). A Hydromechanical Representation of Rock Fractures, A.A. Balkema. Permission to Distribute - American Rock Mechanics Association.

Rahman, M. K., M. M. Hossain and S. S. Rahman (2000). "An analytical method for mixed-mode propagation of pressurized fractures in remotely compressed rocks." International Journal of Fracture **103**(3): 243-258.

Rahman, M. K., M. M. Hossain and S. S. Rahman (2002). "A shear-dilation-based model for evaluation of hydraulically stimulated naturally fractured reservoirs." International Journal for Numerical and Analytical Methods in Geomechanics **26**(5): 469-497.

Rayner, B. L. (1995). "Palm Valley 10 and 10A FMS Interpretation Report." Schlumberger, for Magellan Petroleum Australia Limited (unpublished): 762-774.

Voss, R. F. (1985). Random fractal forgeries. Fundamental algorithms for computer graphics, Springer**:** 805-835.

Warpinski, N., S. Wolhart and C. Wright (2004). "Analysis and prediction of microseismicity induced by hydraulic fracturing." SPE Journal **9**(01): 24-33.

Watanabe, N. (2012). Finite element method for coupled thermo-hydro-mechanical processes in discretely fractured and non-fractured porous media, PhD Thesis, Technische Universität Dresden, Chair of Applied Environmental System Analysis, Helmholtz Centre for Environmental Research UFZ, Department of Environmental Informatics.

Watanabe, N., W. Wang, C. McDermott, T. Taniguchi and O. Kolditz (2010). "Uncertainty analysis of thermo-hydro-mechanical coupled processes in heterogeneous porous media." Computational Mechanics 45(4): 263-280.

Willis-Richards, J., K. Watanabe and H. Takahashi (1996). "Progress toward a stochastic rock mechanics model of engineered geothermal systems." J. Geophys. Res. 101(B8): 17481-17496.

Woodbury, A. and K. Zhang (2001). "Lanczos method for the solution of groundwater flow in discretely fractured porous media." Advances in Water Resources 24(6): 621-630.

Zimmerman, R. and G. Bodvarsson (1996). "Hydraulic conductivity of rock fractures." Transport in Porous Media 23(1): 1-30.

Appendix: Effective Permeability Tensor Calculations

Three-dimensional flow equations used for permeability-tensor calculations are given by Darcy's law and continuity equation as:

$$\begin{Bmatrix} u_x \\ u_y \\ u_z \end{Bmatrix} = \begin{bmatrix} k_{xx} & k_{xy} & k_{xz} \\ k_{yx} & k_{yy} & k_{yz} \\ k_{zx} & k_{zy} & k_{zz} \end{bmatrix} \begin{Bmatrix} \frac{\partial p}{\partial x} \\ \frac{\partial p}{\partial y} \\ \frac{\partial p}{\partial z} \end{Bmatrix} \tag{A-1}$$

$$\nabla . u = 0.0 \tag{A-2}$$

where u is the fluid velocity vector. Periodic boundary conditions are required for solving all elements of permeability tensor in Eq. (1). Periodic boundary condition was proposed by Durlofsky (1991) by assuming a constant pressure gradient along one direction with zero pressure gradients in all other directions, as shown in Eqs. (3), (4) and (5) shows.

$$\mathrm{v}_x = -k_{xx}\frac{\partial p}{\partial x} - k_{xy}\frac{\partial p}{\partial y} - k_{xz}\frac{\partial p}{\partial z} \tag{A-3}$$

$$\mathrm{v}_y = -k_{yx}\frac{\partial p}{\partial x} - k_{yy}\frac{\partial p}{\partial y} - k_{yz}\frac{\partial p}{\partial z} \tag{A-4}$$

$$\mathrm{v}_z = -k_{zx}\frac{\partial p}{\partial x} - k_{zy}\frac{\partial p}{\partial y} - k_{zz}\frac{\partial p}{\partial z} \tag{A-5}$$

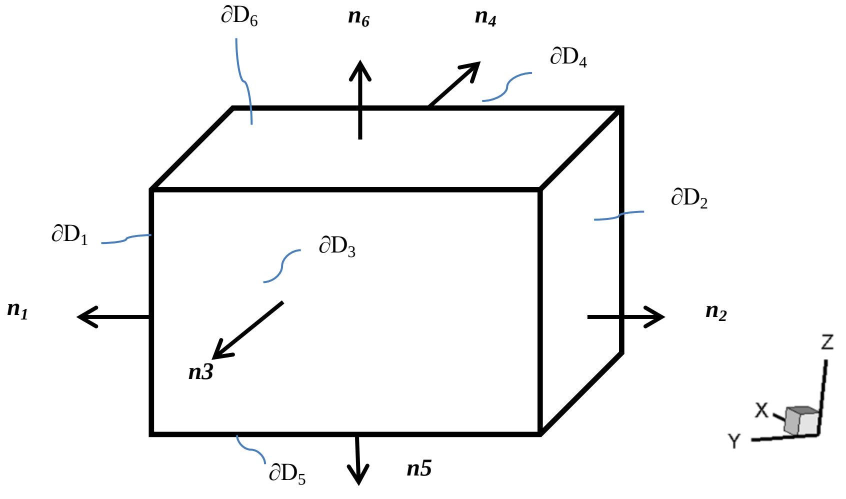

Fig.A-1: Periodic boundary conditions used to calculate elements of permeability tensor in a three-dimensional space by using single-phase flow model.

Pressure and flux boundaries are specified in Eq. (6-11). By specifying a zero pressure gradient along the other faces ($\frac{\partial p}{\partial y}$=0.0, $\frac{\partial p}{\partial z}$=0.0) three elements of permeability tensor can be determined as follows:

$$P\ (y, x=0, z) = P\ (y, x=1, z) \qquad \text{on } \partial D_3 \text{ and } \partial D_4 \tag{A-6}$$

$$u\ (y, x=0, z) \bullet \boldsymbol{n_3} = -u\ (y, x=1, z) \bullet \boldsymbol{n_4} \qquad \text{on } \partial D_3 \text{ and } \partial D_4 \tag{A-7}$$

$$P\ (y=0, x, z) = P\ (y=1, x, z) - \boldsymbol{G} \qquad \text{on } \partial D_1 \text{ and } \partial D_2 \tag{A-8}$$

$$u\ (y=0, x, z) \bullet \boldsymbol{n_1} = -u\ (y=1, x, z) \bullet \boldsymbol{n_2} \qquad \text{on } \partial D_1 \text{ and } \partial D_2 \tag{A-9}$$

$$P\ (y, x, z=0) = P\ (y, x, z=1) \qquad \text{on } \partial D_5 \text{ and } \partial D_6 \tag{A-10}$$

$$u\ (y, x, z=0) \bullet \boldsymbol{n_5} = -u\ (y, x, z=1) \bullet \boldsymbol{n_6} \qquad \text{on } \partial D_6 \text{ and } \partial D_6 \tag{A-11}$$

where n is the outward normal vector at the boundaries, and G is the pressure gradient. The rest of permeability-tensor elements can be calculated by specifying the same boundary conditions as above-mentioned, but in the opposite directions.

The effective permeability of fractured reservoir has been calculated by using finite element technique. Each fracture is represented as a sandwiched two dimensional element (triangular) between three dimensional elements (tetrahedral) representing the matrix porous medium as shown in Figure A-1.

Single phase steady state fluid-flow in matrix can be written as follows:

$$\nabla .\left(\frac{\overset{\rightrightarrows}{k}}{\mu}.\nabla p\right)+Q_H=0.0 \tag{A-12}$$

$$\mathbf{v} = -\left(\frac{\overset{\rightrightarrows}{k}}{\mu}\nabla p\right) \tag{A-13}$$

where $\overset{\rightrightarrows}{k}$ is a full permeability tensor, μ is the fluid viscosity, Q_H is fluid source/sink term which represents the fluid exchange between matrix and fracture, or fluid extraction (injection) from the wellbore. Fluid-flow in a single fracture is also expressed as follows:

$$\overline{\nabla}.\left(\frac{k_f}{\mu}\nabla p_f\right)+q^{+}+q^{-}=0.0 \tag{A-14}$$

where q^{+} and q^{-} are the leakage fluxes across the boundary interfaces, $\overline{\nabla}$ is the divergence operator in local coordinates system (Watanabe et al. 2010), and Pf is the pressure inside the fracture. The permeability of the fracture can be expressed by a parallel plate concept (cubic law) as shown in Eq. 23. It has been assumed that the fracture surfaces are parallel and the fluid-flow through a single discrete fracture is laminar (Snow 1969).

$$k_f = \frac{b^2}{12} \tag{A-15}$$

where b is the fracture aperture, and k_f is the fracture permeability.

The weighted-residual method is then used to derive the weak formulation of the governing equation of fluid-flow through a fractured system, and the standard Galerkin method was applied to discretise the weak forms with appropriate boundary conditions (Zimmerman and Bodvarsson 1996, Woodbury and Zhang 2001).

Equations (12) and (14) are written separately for the matrix and fractures. The matrix is discretised using 3D elements and fractures are discretised by using 2D elements. If CFEQ represents the control flow equations (12) and (14), the integral form of the flow equations for discrete fracture model can be written as

$$\int\int_{\Omega} \text{CFEQ}\ d\Omega = \int\int_{\Omega_m} \text{CFEQ}\ d\Omega_m + \boldsymbol{b} \text{ x } \int\int_{\Omega_f} \text{CFEQ}\ d\overline{\Omega}_f \tag{A-16}$$

where $\overline{\Omega}_f$ represents the fracture part of the domain as a 2D entity, and Ω_m represents matrix domain and Ω is the entire domain. 2D integral fracture equation is multiplied by the fracture aperture b for consistency of the integral form.

The finite element formulation of the governing equation for hydraulic process in matrix and fracture can be written in the matrix form as:

$$\left[\overset{\rightrightarrows}{M}\right][\overrightarrow{\Delta p}]=\vec{f} \tag{A-17}$$

$$\overset{\rightrightarrows}{M} = \overrightarrow{\overrightarrow{M_1{}^m}}+\overrightarrow{\overrightarrow{M_2{}^f}} \tag{A-18}$$

$$\overset{\rightrightarrows}{M} = \int_{\Omega} \nabla N_p^{m^T}\ \frac{k}{\mu}\ \nabla N_p^m\ d\Omega + \int_{\Gamma} \nabla N_p^{f^T}\ \left(\frac{b \text{ x } k}{\mu}\right)\ \nabla N_p^f\ d\Gamma \tag{A-19}$$

$$\vec{f} = -\int_{\Gamma} N_p^{m^T}\ Q_H\ d\Gamma - \overrightarrow{\overrightarrow{M_1{}^m}}\ \vec{P}^{i-1^m} - \overrightarrow{\overrightarrow{M_2{}^f}}\ \vec{P}^{i-1^f} - \int_{\Gamma} N_p^{f^T}\ Q_H\ d\Gamma \qquad \text{(A-20)}$$

where N is the corresponding shape function for the matrix and fracture elements and, and Γ is a domain boundary.

After using these equations for pressure calculations, the average velocity for each reservoir block in x, y and z directions can be calculated by using Eq. (21-23) as:

$$\langle v_x \rangle = -\int_{\partial D_3} \mathbf{v}.\mathbf{n}_3\ dx\ dz \qquad \text{(A-21)}$$

$$\langle v_y \rangle = -\int_{\partial D_1} \mathbf{v}.\mathbf{n}_1\ dy\ dz \qquad \text{(A-22)}$$

$$\langle v_z \rangle = -\int_{\partial D_5} \mathbf{v}.\mathbf{n}_5\ dx\ dy \qquad \text{(A-23)}$$

Full permeability tensor components can then be obtained as mentioned before by using Eqs. (3-5).

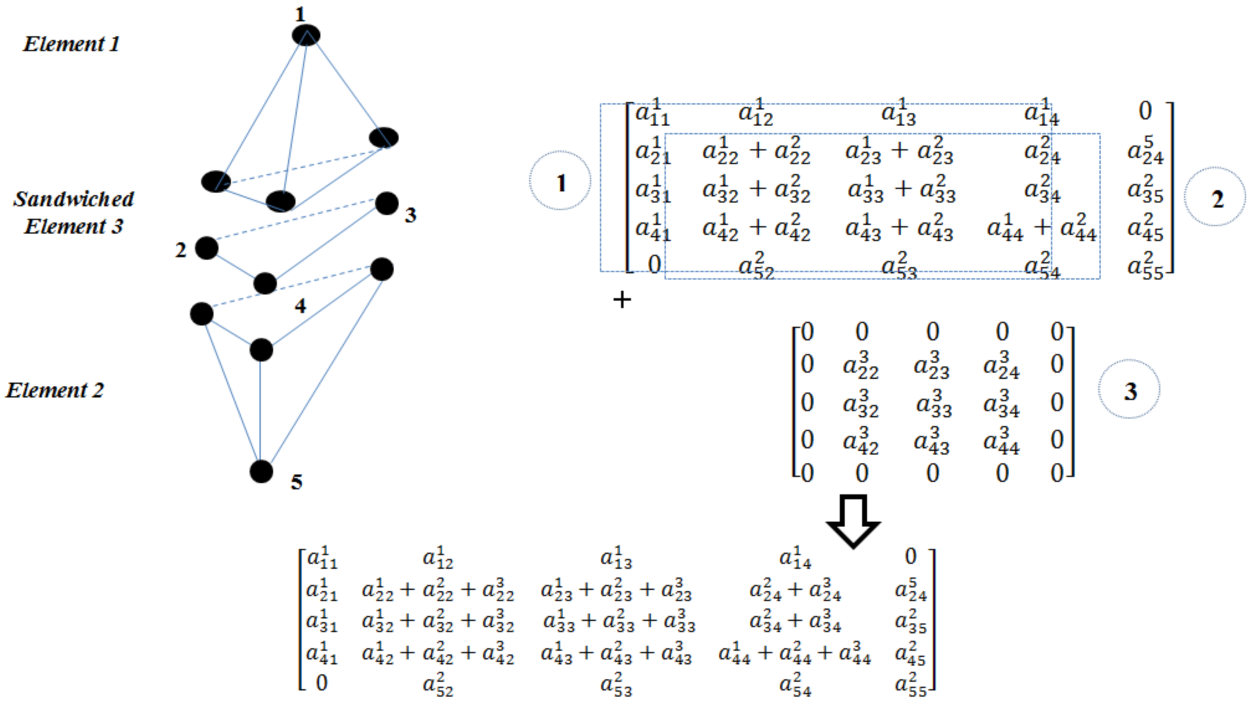

$$\begin{bmatrix} a_{11}^1 & a_{12}^1 & a_{13}^1 & a_{14}^1 & 0 \\ a_{21}^1 & a_{22}^1 + a_{22}^2 & a_{23}^1 + a_{23}^2 & a_{24}^2 & a_{24}^5 \\ a_{31}^1 & a_{32}^1 + a_{32}^2 & a_{33}^1 + a_{33}^2 & a_{34}^2 & a_{35}^2 \\ a_{41}^1 & a_{42}^1 + a_{42}^2 & a_{43}^1 + a_{43}^2 & a_{44}^1 + a_{44}^2 & a_{45}^2 \\ 0 & a_{52}^2 & a_{53}^2 & a_{54}^2 & a_{55}^2 \end{bmatrix} + \begin{bmatrix} 0 & 0 & 0 & 0 & 0 \\ 0 & a_{22}^3 & a_{23}^3 & a_{24}^3 & 0 \\ 0 & a_{32}^3 & a_{33}^3 & a_{34}^3 & 0 \\ 0 & a_{42}^3 & a_{43}^3 & a_{44}^3 & 0 \\ 0 & 0 & 0 & 0 & 0 \end{bmatrix}$$

$$\Downarrow$$

$$\begin{bmatrix} a_{11}^1 & a_{12}^1 & a_{13}^1 & a_{14}^1 & 0 \\ a_{21}^1 & a_{22}^1 + a_{22}^2 + a_{22}^3 & a_{23}^1 + a_{23}^2 + a_{23}^3 & a_{24}^2 + a_{24}^3 & a_{24}^5 \\ a_{31}^1 & a_{32}^1 + a_{32}^2 + a_{32}^3 & a_{33}^1 + a_{33}^2 + a_{33}^3 & a_{34}^2 + a_{34}^3 & a_{35}^2 \\ a_{41}^1 & a_{42}^1 + a_{42}^2 + a_{42}^3 & a_{43}^1 + a_{43}^2 + a_{43}^3 & a_{44}^1 + a_{44}^2 + a_{44}^3 & a_{45}^2 \\ 0 & a_{52}^2 & a_{53}^2 & a_{54}^2 & a_{55}^2 \end{bmatrix}$$

Fig. A-2: Description of how the whole matrix for 3D space of fractures and rock matrix elements constructed to be used during the simulation process.